



Surfactant spreading on a thin liquid film: reconciling models and experiments

Ellen R. Swanson · Stephen L. Strickland ·
Michael Shearer · Karen E. Daniels

Received: 20 June 2013 / Accepted: 24 July 2014 / Published online: 23 October 2014
© Springer Science+Business Media Dordrecht 2014

Abstract The spreading dynamics of surfactant molecules on a thin fluid layer is of both fundamental and practical interest. A mathematical model formulated by Gaver and Grotberg [J Fluid Mech 235:399–414, 1992] describing the spreading of a single layer of insoluble surfactant has become widely accepted, and several experiments on axisymmetric spreading have confirmed its predictions for both the height profile of the free surface and the spreading exponent (the radius of the circular area covered by surfactant grows as $t^{1/4}$). However, these prior experiments utilized primarily surfactant quantities exceeding (sometimes far exceeding) a monolayer. In this paper, we report that this regime is characterized by a mismatch between the timescales of the experiment and model and, additionally, find that the spatial distribution of surfactant molecules differs substantially from the model prediction. For experiments performed in the monolayer regime for which the model was developed, the surfactant layer is observed to have a spreading exponent of less than 1/10, far below the predicted value, and the surfactant distribution is also in disagreement. These findings suggest that the model is inadequate for describing the spreading of insoluble surfactants on thin fluid layers.

Keywords Experiment · Model · Surfactant · Thin liquid film

1 Introduction

Axisymmetric spreading of an insoluble surfactant on a thin layer of incompressible fluid has been the subject of numerous experimental and mathematical studies [1–6]. Motivated by the biomedical application of aerosol medications delivered to the thin fluid lining the lung, Gaver and Grotberg [4] derived a mathematical model, based on lubrication theory, that couples the height profile of a fluid surface $h(r, t)$ to the local surfactant concentration $\Gamma(r, t)$. The model dynamics are driven by the force associated with the Marangoni surface stress, as induced by

E. R. Swanson (✉)
Department of Mathematics, Centre College, Danville, KY 40422, USA
e-mail: ellen.swanson@centre.edu

S. L. Strickland · K. E. Daniels
Department of Physics, North Carolina State University, Raleigh, NC 27695, USA

M. Shearer
Department of Mathematics, North Carolina State University, Raleigh, NC 27695, USA

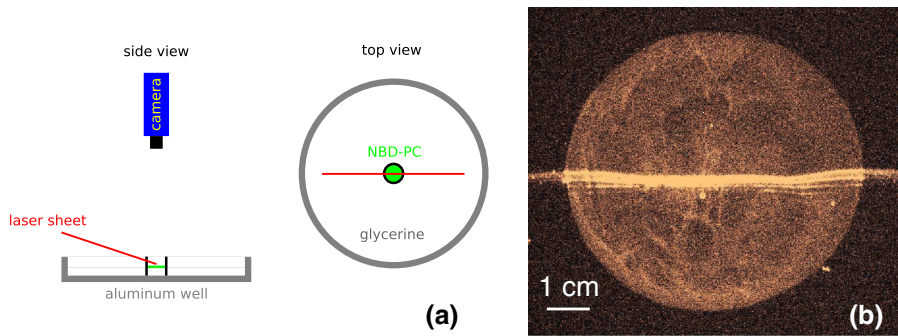


Fig. 1 **a** Schematic of apparatus. **b** Sample image from experiments with initial conditions IC5, with both height profile (*bright line*) and fluorescence signal from NBD-PC lipids (*bright disk*) at $t^* = 21$ s

spatial variations in surfactant concentration. This in turn depends on an equation of state that specifies the surface tension σ as a function of Γ . While the model was developed for monolayer applications of surfactant, it has come to be applied both above [2] and near [1] the critical monolayer concentration Γ_c , the concentration above which a single layer of surfactant molecules can no longer form. Similar models have been used to study thin films in bronchial systems [7], ocular systems including blinking dynamics [8], bulk solute transport [9], drying of latex paint [10–12], ink-jet printing [13], and secondary oil recovery [14, 15].

The goal of this paper is to examine whether the aforementioned model accurately predicts both the motion of underlying fluid and the spreading of a surfactant. While we find some features of the experimental results to be in agreement with the model, some are not, and we provide detailed comparisons to establish the inadequacies of the model equations. Numerical simulations are used to confirm several predictions of the model [6, 16] based on an analysis of self-similar solutions. The simulations also yield detailed information about the spatiotemporal evolution of the free-surface height and surfactant concentration profiles. One key observation is that the decrease in surfactant concentration at the leading edge induces a Marangoni stress there and drives a capillary ridge (local maximum) in the fluid-free surface that propagates along with the leading edge.

Despite these advances in understanding, experimental confirmation of the model has been hindered by the difficulty of measuring the surfactant concentration and its dynamics. Consequently, attention has focused primarily on the evolution of the surface height profile [1, 2, 17], with the location of the leading edge r_0 of the surfactant layer inferred from other dynamics [1]. Within the near-monolayer regimes for which the model was developed, two experiments have observed $r_0(t) \propto t^{0.6-0.8}$ spreading behavior on millimetric glycerin films, for both oleic acid [18] and fluorescently tagged phosphocholine (NBD-PC) [1]. In experiments with initial concentrations $\bar{\Gamma}_0$ of surfactant exceeding Γ_c , spreading behavior consistent with the predicted $r_0(t) \propto t^{1/4}$ was observed by Dussaud et al. [2] for oleic acid on a submillimetric water-glycerin mixture, and by Fallest et al. [3] for NBD-PC on millimeter-thick glycerin. The latter experiments were able to simultaneously measure both the capillary ridge and the spatiotemporal dynamics of $\Gamma(r, t)$, to be analyzed in more detail subsequently.

We explore stricter tests of the model than have been performed previously, specifically in exploration of the time-dependent distribution of the surfactant concentration. Using data from Fallest et al. [3] (for which Γ is well above Γ_c), we make a detailed comparison between the model predictions and the measured surface height profiles $h(r, t)$ (from a laser line) and measured surfactant concentration profiles $\Gamma(r, t)$ (from azimuthal averages of fluorescent intensity at each point \vec{r}). Figure 1 provides a schematic of the apparatus and a sample image. The well-specified physical parameters additionally allow us to evaluate the accuracy of the characteristic timescale predicted for the spreading rate, rather than just the exponent. While we find approximate agreement in the spreading exponent and the coincidence of the surfactant leading edge with the capillary ridge, we also find two significant inconsistencies. First, there is a mismatch between the characteristic timescale between model and experiment. Second, the spatial distribution of the surfactant differs markedly from what is predicted in simulations. To account for the extent to which these discrepancies might be due to amounts of surfactant well beyond the monolayer regime, we perform

new experiments, modified to allow for the detection of monolayer concentrations of surfactant ($\Gamma < \Gamma_c$). In these experiments, we observe a distribution of surfactant that differs from the model predictions. In addition, we find that there is no spreading capillary ridge and that the spreading exponent for the leading edge of the surfactant is less than 1/10. This value is well below predictions of the theory.

The outline of the paper is as follows. In Sect. 2, we provide details about the experimental setup and the materials used. In Sect. 3, we review the Gaver–Grotberg model [4], including a discussion of the choice of equation of state relating surfactant concentration to surface tension and outline the finite-difference method used for numerical simulation. In Sect. 4, we describe comparisons between numerical simulations and experimental results at initial concentrations well above Γ_c . As described previously, we find partial agreement but also two inconsistencies when comparing experimental observations to numerical simulations. In an attempt to address the latter problem, in Sect. 5 we describe a hybrid model that takes the experimentally measured $\Gamma(r, t)$ and uses that quantity (instead of the model for surfactant evolution) to generate the evolution of the surface height profile. We find that this provides reasonable agreement with the experimental data for $h(r, t)$. In particular, the timescale in the simulations is set by the experimental surfactant distribution, and the height profile dynamics therefore evolve according to the experimentally observed timescale. In Sect. 6, we report new experiments with $\Gamma < \Gamma_c$ and find significant disagreement with the model predictions, as summarized earlier. We conclude in Sect. 7 with a discussion of the results and their significance.

2 Surfactant-spreading experiments

In our experiments, we simultaneously record the surface height profile $h^*(r, t)$ of the underlying glycerin fluid layer and the local fluorescence intensity, which corresponds to the local concentration $\Gamma^*(\vec{r}, t)$ of insoluble lipids (surfactant) spreading on the surface. We use laser profilometry [3] to measure the fluid height profile via a laser sheet pointed at an oblique angle toward the center of the surfactant-spreading system. An example image and schematic are shown in Fig. 1. Any vertical deviation of the fluid surface linearly shifts the optical location of the laser line by an amount proportional to the deviation. We visualize this shift of the laser line with a camera positioned directly above the system. The basic apparatus used to collect the data presented in Sect. 4 utilizes a cylindrical aluminum well to hold the fluid layer, a red laser line, a black light for exciting the NBD fluorophore, and a digital camera; this apparatus is identical to the one used in [3]. Further experiments, presented in Sect. 6, are optimized to permit visualization of monolayer concentrations of surfactant. The bottom of the aluminum well is covered with a plasma-cleaned silicon wafer for improved reflectivity, and the fluorescent excitation is provided by 467 nm Blue LEDs (from Visual Communications Company, LLC) which coincide with the 464 nm absorption peak of the NBD fluorophore. Both the fluorescence signal from the lipids and the reflection from the Green Laser (from Laser Glow) used for profilometry pass through a Bandpass Filter (from Newport) centered at the emission peak (531 nm) of the fluorescence. These improvements to the optics over those in [3] permit us to collect images of the spreading dynamics at a frame rate of 3 Hz and an integration time of 1/4 s, using an Andor Luca R camera optimized for fluorescence measurements. The signal-to-noise ratio now sets a lower limit of $\mathcal{O}(10^{-2})\Gamma_c$ for the detection of surfactant.

For all experiments, we deposit 1-palmitoyl-2-{12-[(7-nitro-2-1, 3-benzoxadiazol-4-yl)amino]lauroyl}-sn-glycero-3-phosphocholine (abbreviated NBD-PC, from Avanti Polar Lipids) within a retaining ring that is lifted to begin the spreading process. This lipid molecule has one 12-carbon chain and one 16-carbon chain; the NBD fluorophore is attached to the 12-carbon chain. Experiments are conducted on a layer of Glycerin (from Sigma Aldrich) of depth $d = (0.98 \pm 0.03)$ mm. The room temperature is (22.5 ± 1.5) °C, and the humidity ranges from 19 to 50 %, depending on atmospheric conditions. The glycerin is allowed to equilibrate for 2 h before the experiments, during which time hygroscopic effects from the ambient humidity could reduce the viscosity of the glycerin. Possible implications of this effect are discussed in Sect. 4.1. The lipids are initially deposited while dissolved in chloroform, which is allowed to evaporate for at least 30 min before the retaining ring is lifted by a motor at 1 mm/min. This allows sufficient time for the meniscus to drain before it detaches from the ring.

Table 1 Key dimensional parameters

Symbol	Interpretation	Value
ρ	Fluid density, 99.5 % anhydrous glycerin	1.26 g/cm ³
μ	Dynamic viscosity, 99.5 % anhydrous glycerin	0.83 ± 0.03 Pas [19]
D_s	Surface diffusivity, surfactant	10 ⁻⁴ cm ² /s [20]
σ_0	Surface tension, clean glycerin	63.4 ± 0.3 dyne/cm [21]
σ_m	Surfactant-contaminated surface tension	35.3 ± 0.3 dyne/cm [1]
S	Change in surface tension, $S = \sigma_0 - \sigma_m$	28.1 ± 0.06 dyne/cm
Γ_c	Critical monolayer concentration	0.3 μg/cm ² [1]
H_0	Initial fluid thickness	0.98 ± 0.03 mm
R_0	Lateral dimension	0.8 or 1.4 cm (ring radius)
L_0	Radius of aluminum well	11.1 or 14.6 cm

Table 2 Six different initial conditions for experiments presented in present paper

	M_L (μg)	R_0 (cm)	$\bar{\Gamma}_0^*$ (μg/cm ²)	
IC1	0.85	1.4	0.13	$\bar{\Gamma}_0^* < \Gamma_c$
IC2	1.4	1.4	0.22	
IC3	1.7	1.4	0.26	
IC4	0.6	0.8	0.30	
IC5	18.0	1.4	2.73	$\bar{\Gamma}_0^* > \Gamma_c$
IC6	18.0	0.8	8.95	

The key material parameters for NBD-PC and glycerin are summarized in Table 1. The initial conditions (ICs) for the experiment are distinguished by the initial concentration $\bar{\Gamma}_0^*$ of surfactant deposited within the ring, defined by

$$\bar{\Gamma}_0^* \equiv \frac{M_L}{\pi R_0^2}, \quad (1)$$

where M_L is the mass of NBD-PC deposited and R_0 is the radius of the ring. Although a small amount of surfactant remains on the ring after it has been lifted, we nonetheless use the nominal concentration $\bar{\Gamma}_0^*$ to describe the different initial conditions in Table 2. The experiments presented in Sect. 4 all begin from IC6, with $\bar{\Gamma}_0^*$ above the critical monolayer concentration Γ_c . The experiments presented in Sect. 6 employ ICs that probe the monolayer regime (below Γ_c).

Figure 1b shows a sample image of both the laser line [measures the height profile $h^*(r)$ and the location r_M of its maximum] and the fluorescence intensity [measures the surfactant distribution $\Gamma^*(r)$ after azimuthal averaging and the location r_0 of its leading edge]. Figure 2 shows sample images of the surfactant distribution alone for a representative $\bar{\Gamma}_0^* > \Gamma_c$ case and a $\bar{\Gamma}_0^* < \Gamma_c$ case. In each image, a sharp interface between the surfactant-covered and bare glycerin is readily visible; the location r_0 of this interface is determined by identifying the annulus of the maximum fluorescence intensity gradient. While the surfactant distribution is uniform for $\bar{\Gamma}_0^* < \Gamma_c$, several heterogeneities are present when $\bar{\Gamma}_0^* > \Gamma_c$. First, the central region contains a greater concentration of surfactant than the regions closer to the leading edge, an effect that we will explore in more detail below. Second, there are filamentary patches of high concentration that also propagate out from the central region, becoming more dilute during the spreading dynamics. We also note that the outer edge of surfactant in both cases has corrugations; in the figure, white circles are imposed to emphasize that the edges are not quite circular. Although the surfactant

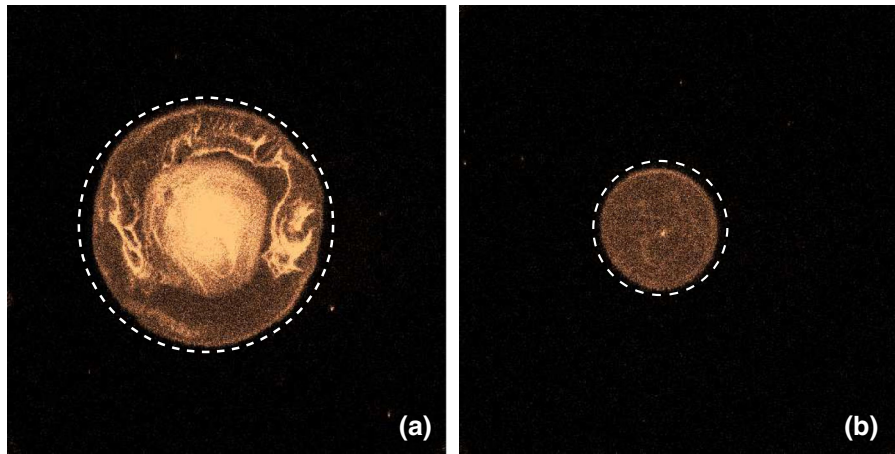


Fig. 2 Fluorescence intensity (proxy for surfactant concentration), measured at $t^* = 5$ s, for experiments with ICs **a** IC6 and **b** IC4. The dashed circles (of radii 3.4 and 1.1 cm, respectively) highlight the corrugations in the leading edge

distributions are never precisely axisymmetric, we nonetheless record the distribution by azimuthal averaging. Moreover, in the model and simulations of the following sections, we assume that the surfactant distributions are axisymmetric.

3 Model

We consider the model derived by Gaver and Grotberg [4] for a single layer of surfactant molecules spreading on a thin liquid film. The model is a coupled system of partial differential equations for the height $h(r, t)$ of the fluid-free surface and the concentration $\Gamma(r, t)$ (mass per unit area) of surfactant. We assume axisymmetric spreading, and the variables are nondimensionalized: $r = r^*/R$, $t = t^*/T$, $h = h^*/H_0$, $\Gamma = \Gamma^*/\Gamma_c$, where $*$ indicates the dimensional variable:

$$h_t + \frac{1}{r} \left(\frac{1}{2} rh^2 \sigma(\Gamma)_r \right)_r = \beta \frac{1}{r} \left(\frac{1}{3} rh^3 h_r \right)_r - \kappa \frac{1}{r} \left(\frac{1}{3} rh^3 \left(h_{rr} + \frac{1}{r} h_r \right)_r \right)_r, \quad (2a)$$

$$\Gamma_t + \frac{1}{r} (rh\Gamma\sigma(\Gamma)_r)_r = \beta \frac{1}{r} \left(\frac{1}{2} rh^2 \Gamma h_r \right)_r - \kappa \frac{1}{r} \left(\frac{1}{2} rh^2 \Gamma \left(h_{rr} + \frac{1}{r} h_r \right)_r \right)_r + \delta \frac{1}{r} (r\Gamma_r)_r. \quad (2b)$$

The values for the nondimensional parameter groups β , κ , and δ are obtained using values of physical parameters listed in Table 1. The parameter $\beta = \rho g H_0^2 / S \approx 0.42$ balances gravity and Marangoni forces, $\kappa = \sigma_m H_0^2 / (S R_0^2) \approx 0.019$ is the ratio of the capillary driving forces to the forces from the surface tension gradient, and $\delta = 1/\text{Pe} = \mu D / (S H_0) \approx 3.0 \times 10^{-5}$ represents the surface diffusion of the surfactant molecules, where Pe is the Péclet number. The function $\sigma(\Gamma)$ expresses the dependence of surface tension σ on surfactant concentration Γ . It is specified by an equation of state, as discussed in the next subsection. The timescale $T = \mu R_0^2 / (S H_0) \approx 2.0$ s achieves a balance between the terms on the left-hand side of (2). In Sect. 4.1, we test this predicted timescale directly.

With $\delta > 0$, the leading edge of the surfactant distribution is not precisely defined since $\Gamma(r, t) > 0$ for all r and for all $t > 0$. Nonetheless, although δ is very small, it is generally retained in numerical simulations. However, for the purpose of tracking the leading edge of the surfactant distributions, δ is set to zero.

At $r = 0$ the no-flux boundary condition, which is consistent with radial symmetry, is enforced; for large r , the free surface is undisturbed on the timescale of the experiment, and the surfactant concentration is expected to be identically zero:

$$h_r(0, t) = \Gamma_r(0, t) = 0, \quad h_{rr}(0, t) = 0, \quad \lim_{r \rightarrow \infty} h(r, t) = 1, \quad \lim_{r \rightarrow \infty} \Gamma(r, t) = 0. \quad (3)$$

A finite-difference method is used to simulate (2) and is summarized in the appendix. The initial condition $h(r, 0)$ is chosen to reflect the initial height profile in the experiment as the fluid meniscus detaches from the ring, thereby releasing the surfactant to spread across the fluid surface. Because the ring partially obscures the camera view, the first usable images occur shortly after the meniscus has detached and the spreading has commenced. Therefore, we choose initial conditions to be consistent with this first usable image. In some experiments, the laser line extends across the entire system. In others, the laser line extends only across half of the system in order to facilitate better imaging of the initial surfactant concentration. In some experiments, the $h(r)$ profiles near $r \approx 1$ to allow as many pixels from the digitized image as possible to be included in the fluorescence profile. Consequently, the initial distribution $\Gamma_0(r)$ of surfactant within the ring is unknown from experiments and will be varied in the simulations to test its effect on the spreading:

$$\begin{aligned} h(r, t_0) &= \begin{cases} a \sin(2r - \frac{\pi}{3}) + (1+a) & 0 \leq r < \frac{11\pi}{12}, \\ 1 & \frac{11\pi}{12} < r < R_{\max}, \end{cases} \\ \Gamma(r, t_0) &= \begin{cases} \Gamma_0(r) & 0 \leq r < \frac{5\pi}{12}, \\ 0 & \frac{5\pi}{12} < r < R_{\max}, \end{cases} \end{aligned} \quad (4)$$

where t_0 is the time of the first usable image. The empirical parameters are chosen as follows: the distorted portion of the free-surface height $h(r, t_0)$ is located in the interval $0 \leq r \leq 11\pi/12$, whereas the edge of the surfactant layer has reached $r(t_0) = 5\pi/12$. We observe that $h(r, t_0)$ is continuous at $r = 11\pi/12$ and has a maximum at $r = 5\pi/12$, as shown in Fig. 3. The location R_{\max} of the edge of the computational domain is taken large enough that the numerical influence of the boundary conditions at $r = R_{\max}$ is negligible over the time of the experiment. We take $R_{\max} = 10$, which is approximately the nondimensional radius L_0/r_0 of the cylindrical well, but display graphs of h and Γ over the smaller domain, $0 \leq r \leq 7$.

3.1 Equation of state

To compare the model (2) to the results of the experiments described in [3], we need to choose an appropriate equation of state relating the surfactant concentration Γ to the surface tension σ . However, the model is valid only for a single layer of surfactant molecules ($\Gamma \leq 1$), and the experiments are conducted with initial surfactant concentrations of up to $\Gamma = 30$. This large amount of surfactant may cause the surfactant to exhibit other phases including solubility. Models that incorporate solubility are explored in [22–24]. Here, we extend the equation of state for an insoluble surfactant to the regime of the experiment and consider various equations of state $\sigma = \sigma(\Gamma)$ that have been proposed in the literature. In Fig. 4, we show the graphs of four such functions, and in what follows we argue that only the curve labeled M is suitable for modeling the full range of surfactant concentrations we wish to consider.

The equation of state we seek should have the following properties: $\sigma'(\Gamma) < 0$, expressing the effect that an increasing surfactant concentration decreases the surface tension; $0 < \sigma(\Gamma) \leq 1$, since this is the range of values of surface tension in our nondimensionalization, with $\sigma(0) = 1$. As can be seen in the figure, only curve M has these properties.

The linear equation of state

$$\sigma(\Gamma) = 1 - m\Gamma, \quad (5)$$

has been used widely [24–27]. This equation is generally chosen for simplicity; it is also a reasonable linear approximation to nonlinear equations of state at low concentration. Note that $d\sigma(\Gamma)/d\Gamma = -m$ is a negative constant ($m = 1$ in curve L in Fig. 4). In the case of more than a monolayer of surfactant, this equation suggests that the surface tension decreases endlessly, which is not physical because surfactant concentration beyond a monolayer has little additional effect in decreasing surface tension.

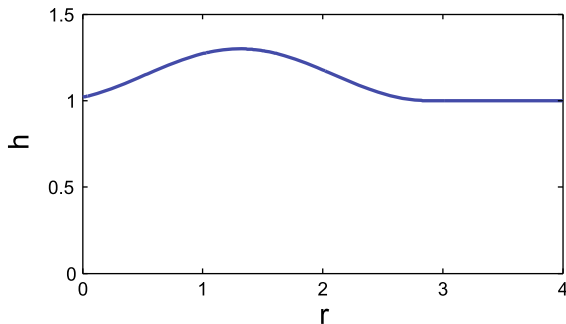


Fig. 3 Initial surface height profile $h(r, 0)$, from (4), used in the simulations. Typical initial conditions for surfactant are shown in Fig. 7

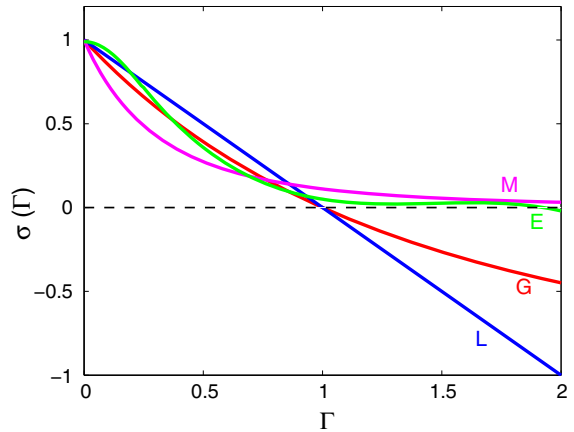


Fig. 4 Four equations of state used in the model: L linear (5), G Langmuir (7), E measured (6), M multilayer (8)

Bull et al. [1] determined an equation of state for NBD-PC on glycerin by fitting the data obtained using a tensiometer. Using the nondimensional parameters in Table 1 ($\Gamma_c \approx 0.3 \text{ } \mu\text{g}/\text{cm}^2$), the corresponding formula for $\sigma(\Gamma)$ is

$$\sigma(\Gamma) = \begin{cases} 0.28 \cos(6.28\Gamma) + 0.71 & \Gamma < 0.25, \\ 1.26 - 2.6\Gamma + 1.8\Gamma^2 - 0.41\Gamma^3 & 0.25 \leq \Gamma \leq 1.67, \end{cases} \quad (6)$$

shown as curve E in Fig. 4. However, this formula is applicable only for surfactant concentrations below approximately $2\Gamma_c$ ($\Gamma < 2$ in Fig. 4), as $\sigma'(\Gamma)$ decreases sharply for larger values of Γ .

The Langmuir equation of state, used in [4] and [28], is

$$\sigma(\Gamma) = \frac{\eta + 1}{(1 + \Theta(\eta)\Gamma)^3} - \eta, \quad (7)$$

where

$$\Theta(\eta) = \left(\frac{\eta + 1}{\eta} \right)^{1/3} - 1 \quad \text{and} \quad \eta = \frac{\sigma_m}{S},$$

($\eta = 1.08$ in curve G in Fig. 4). When only a small amount of surfactant is introduced, a large change in the surface tension occurs, and as the surfactant comes close to saturation (a monolayer), then adding more surfactant does not alter the surface tension significantly. However, the range of $\sigma(\Gamma)$ is $[-\eta, 1]$ rather than $[0, 1]$. The multiple-layer equation of state used by Borgas and Grotberg [29] is related to the Langmuir equation of state:

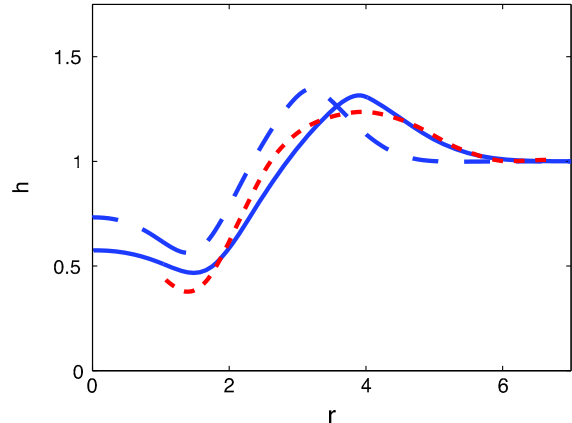
$$\sigma(\Gamma) = (1 + \eta\Gamma)^{-3}, \quad (8)$$

shown as curve M of Fig. 4. This formulation is based on the properties of surface tension discussed by Sheludko [30] and shown by an experimental fit by Foda and Cox [31], who worked with an oil layer on water. In addition, $\sigma(\Gamma)$ remains positive at large Γ , allowing us to simulate much higher concentrations of surfactant. Therefore, we use Eq. (8) for the simulations.

4 High surfactant concentration ($\bar{\Gamma}_0^* > \Gamma_c$)

The $r_0(t) \propto t^{1/4}$ spreading behavior predicted by (2) was already observed in prior experiments with oleic acid on a water–glycerin mixture [2] and NBD-PC on glycerin [3]. In this section, we make a more detailed comparison

Fig. 5 Surface height profiles $h(r)$ measured at $t^* = 5$ s in the experiment (short dashed lines, red), compared to numerical solutions at nondimensional times. Long dashed lines $t = 2.5$ (uses calculated $T = 2.0$ s); solid line $t = 5$ (uses better-fitting $T = 1.0$ s). Data are from Fallest et al. [3], with initial condition IC6++. (Color figure online)



between the results from experiments and numerical simulations using data from Fallest et al. [3]. While we are able to obtain reasonable agreement in the height profile shapes, a comparison of the dynamics (Sect. 4.1) requires that we adjust the timescale. In Sect. 4.2, we show a significant discrepancy between the observed distribution of surfactant and the prediction from simulations, even though the location and time evolution of the leading edge of the surfactant layer agree well, as detailed in Sect. 4.3. We also describe attempts to capture the experimentally observed surfactant distribution by varying the initial distribution $\Gamma_0(r)$ in the simulations.

4.1 Timescale

To compare the model and experiment, we convert the simulation results from dimensionless time t to dimensional time t^* , as discussed in Sect. 3. Previous simulations [2, 18] treated the lengthscale R_0 as a free parameter, effectively adjusting the timescale to agree with the experimental observations. However, for the experiments analyzed here, the ring radius $R_0 = 0.8$ cm is known, and consequently the timescale T is determined, with no free parameters.

In Fig. 5, we observe that the simulated height profile and the experimental data are inconsistent at $t^* = 5$ s if the determined value $T = 2.0$ s is used: neither the peak location nor its width is in agreement with the model. However, if we use $T = 1.0$ s instead of $T = 2.0$ s, thereby comparing the simulation at the later time $t = 5$ to the same experimental data at $t^* = 5$ s, then both the position and width of the ridge are in approximate agreement between the model and experiment. This agreement between simulation and experiment using the timescale $T = 1.0$ s is observed to hold for all times beyond an initial transient.

To resolve this discrepancy, we consider a few possibilities. First, when glycerin absorbs moisture from the air, its viscosity decreases [19, 32]. For our system, such a decrease in viscosity would decrease the timescale T by a humidity-dependent amount, associated with hygroscopic equilibrium. The timescale $T = 2.0$ s reported previously corresponds to 99.5 % anhydrous glycerin (appropriate at 1 % humidity); this timescale would decrease to $T = 0.1$ s at 50 % humidity. To test for this effect, we examined data from [3] for which spreading rates at different humidity values were available. We found no significant correlation between spreading rate and humidity over a range of 19–50 % humidity. This suggests that hygroscopic effects do not significantly affect our observed spreading timescale. A second possibility is that the glycerin becomes contaminated when the lipids are deposited in the chloroform solution. If some chloroform dissolves in the glycerin, this could also cause a decrease in viscosity, similarly affecting T . We note that a similar (but slightly larger) magnitude mismatch in timescale was observed for a related experiment in which lipid spread into a central, clean region [33]. This suggests that the parameters that control T may be more complicated than originally thought. Finally, it may be that other effects not accounted for in this model, such as evaporation and inertia, are significant. However, since the goal of this study is to compare model (2) to the experimental results, we use the empirically determined $T = 1.0$ s as the timescale for the remaining comparisons in the paper.

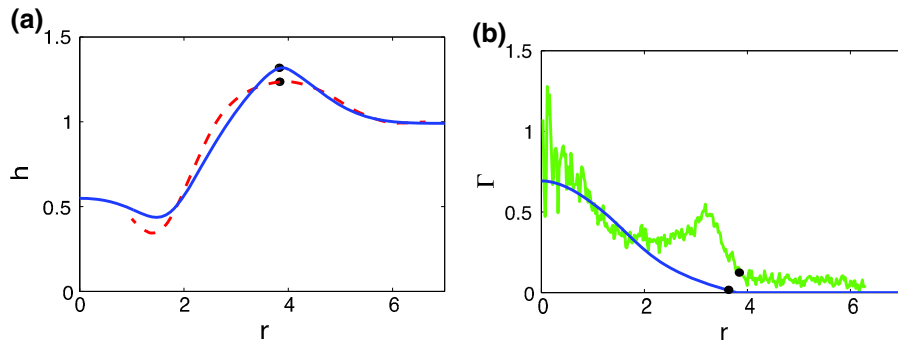


Fig. 6 **a** Surface height profiles $h(r)$ measured at $t^* = 5$ s in experiment (dashed lines) and $t = 5$ in numerical solution (solid line); the location $r = r_M$ of the peak is marked by a bullet symbol. **b** Corresponding surfactant concentration profiles $\Gamma(r)$ in experiment (noisy) and numerical solution (smooth); the location $r = r_0$ of the leading edge of the surfactant is marked by a bullet symbol. Data are from Fallest et al. [3], with initial condition IC6. Note that the larger scatter near the origin is due to the decreasing number of pixels over which the average is taken. The small peak in $I(r)$ near the leading edge arises due to fluorescence resonance energy transfer (FRET) between nearby fluorophores [34]. As a result of FRET, the relationship between fluorescence intensity and surfactant concentration can exhibit nonmonotonic behavior [33]

4.2 Height profile and surfactant distribution

In Fig. 6 we compare the simulated and measured surface profiles and surfactant distributions using the model parameters described in Sect. 4.1 and experimental data from Fallest et al. [3]. As can be seen in Fig. 6, the height profiles $h(r, 5)$ are in approximate agreement: the locations of the maximum and minimum are in approximate agreement between simulation and experiment, and the overall shapes are similar. In contrast, the measured surfactant distribution has quite a different shape from the distribution predicted by the simulations. While the model predicts a smooth decrease in $\Gamma(r, 5)$ away from the central peak, experiments instead show an extended plateau over which the surfactant concentration is nearly constant, and it appears to be drawn out of a reservoir, near the peak concentration at $r = 0$. For longer times, the plateau extends and decreases in height. These features do not appear in the numerical simulations.

However, similar plateaus have been observed in experiments by Vogel and Hirsa [35], who used a different geometry, four different insoluble surfactants, and a different surfactant-detection technique. In their experiments, a monolayer of insoluble surfactant was compressed against a fixed barrier by a flowfield, resulting in a stationary, inhomogeneous surfactant distribution. Their second-harmonic generation optical technique also detected a plateau in surfactant concentration near the leading edge of the front, where the concentration increased from zero. Therefore, similar plateau-like features may be more common than has previously been appreciated.

In our experiment, the total surfactant mass is known, but its initial spatial distribution within the retaining ring is not measured. Consequently, there is some uncertainty about the appropriate initial condition $\Gamma(r, 0) = \Gamma_0(r)$. We explore whether the choice of $\Gamma_0(r)$ could change the simulations enough to replicate the expanding plateau in the experimentally observed surfactant distributions. We tested three different functions Γ_0 , shown in Fig. 7: (a) uniform distribution; (b) surfactant more concentrated near the retaining ring; (c) step distribution. The initial free-surface height profile $h(r, 0)$ is the same in each case, given by (4).

The results of these simulations at time $t^* = 5$ s (after short-time transients have died out) are shown in Fig. 7. In the middle column, we observe that the distribution Γ of surfactant does not exhibit a plateau for any of the initial conditions, while in the final column we see that the height profiles show broad agreement with the experiment in each case.

4.3 Spreading exponent

Despite the aforementioned disagreements, we observe that the spreading dynamics of the model and experiment are in good agreement when the artificial choice of $T = 1$ s is used to scale time. The surface diffusion term $\delta \Gamma_{rr}$

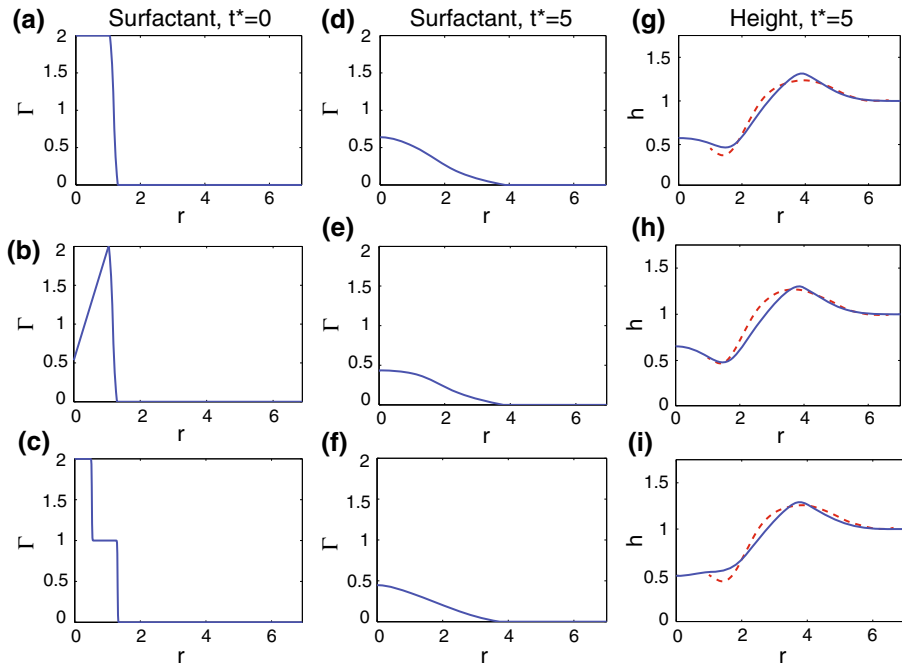


Fig. 7 **a–c** Three different surfactant initial conditions, with the resulting **d–f** surfactant concentration profiles $\Gamma(r)$ and **g–i** surface height profiles $h(r)$ from numerical solutions at $t = 5$. The experimental height profiles resulting from IC6 at $t^* = 5$ s are the same in each case, and are shown as dashed lines

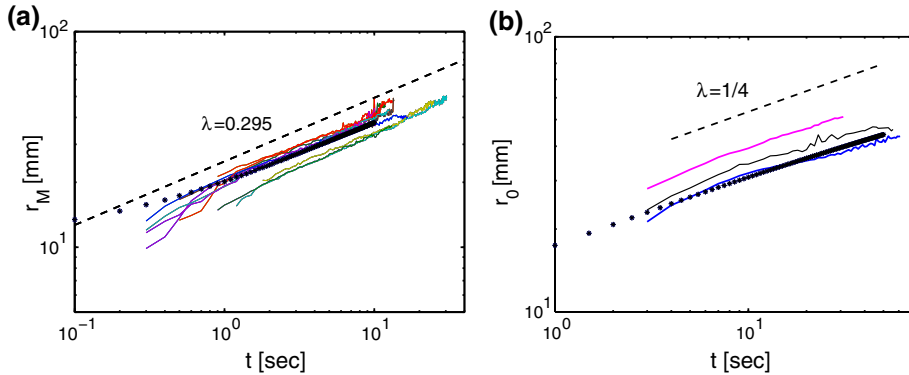


Fig. 8 Comparison between spreading rates of **a** the location of the maximum of the surface height profile $h(r)$ and **b** the location of the leading edge of surfactant in both experiment and simulation. *Colored curves* are from experiments with IC6 adapted from Fallest et al. [3], *black dots* are from simulations, and *dashed curves* denote **a** a comparison to best-fit t^α with $\alpha = 0.295$ and **b** comparison to $t^{1/4}$. (Color figure online)

in (2a) smooths the surfactant profile and guarantees $\Gamma(r, t) > 0$ for all $r \geq 0$ and $t > 0$. This means the surfactant distribution has no clearly defined leading edge but instead drops to nearly zero. Since $\delta \approx 10^{-5}$ has only this very small effect, we take $\delta = 0$ in the simulations that explicitly track the location of the leading edge of the surfactant. The surfactant distribution is then supported at each $t > 0$ on a bounded interval $0 \leq r \leq r_0(t)$, and the leading edge $r = r_0(t)$ can be tracked using the numerical scheme described in [36] with $\beta\kappa > 0$. In Fig. 8b, $r_0(t)$ is shown as a dotted curve; on the log–log plot the numerical solution is compared to the experimental results and to the analytic form $r_0(t) \sim t^{1/4}$ derived from the similarity solution of [6], in which $\beta = \kappa = \delta = 0$.

We also tracked the capillary ridge $r = r_M(t)$, where the height profile $h(r, t)$ has a maximum. In Fig. 8a we show the numerical solution as a dotted curve, and compare it to experimental results, with an approximate slope shown with a dashed curve. The data for the leading edge of the surfactant agrees with the $t^{1/4}$ prediction of the model. The capillary ridge moves faster as it catches up to the surfactant leading edge; it is best fit by $t^{0.295}$ over the duration of the experiment.

Note that for $\beta = \kappa = \delta = 0$ in the model, the fluid surface experiences a discontinuity at the leading edge $r = r_0(t)$ of the surfactant, and the fluid is undisturbed ahead of this front. It is worth noting that with $\delta = 0$, the surfactant distribution still has a finite extent when β or κ is nonzero, but the disturbance of the film does not. In fact, the surface tension gradient induced at the leading edge $r = r_0(t)$ of the surfactant generates fluid motion ahead of r_0 .

5 Hybrid model

Due to the failure of the model equations (2) to capture the spatial distribution of the surfactant, as discussed in Sect. 4, we consider whether there is a fundamental modeling problem with Eq. (2b) for the evolution of $\Gamma(r, t)$. Given that the height profile $h(r, t)$ evolves in a quantitatively reasonable way, we leave (2a) intact but take $\Gamma(r, t)$ from the experiment and use it to determine $h(r, t)$ numerically.

The experimental data for Γ are noisy and occur at discrete times; we must smooth and interpolate the data for use in the numerical scheme to determine h . The first step is to smooth the experimental data at each recording time. This is achieved using MATLAB's *smooth* function, which performs a moving spatial average over a specified span of data points; we found a low-pass filter with a span of 21 data points to be effective; this corresponds to approximately 0.336 cm.

The experimental data are recorded at 1 s intervals and pixels are 0.016 cm wide, the spatial resolution of the camera. However, the numerical method requires the timestep Δt to be on the order of $\mathcal{O}(10^{-3})$ for stability. To remedy this inconsistency, we interpolate the smoothed surfactant profiles to obtain functions that can be used to represent the surfactant concentration $\Gamma(r, t)$ at all values of r and t .

In the first step, we use the nonlinear fit function, *nlinfit*, in MATLAB to fit the smoothed surfactant data at each experimental recording time to a function with a graph consistent with the two-step structure of the experimental surfactant distributions. As observed in Fig. 9, the experimental surfactant distribution Γ is roughly constant in each of the two steps. With this in mind, we use the function

$$\Gamma(r, j) = a_1^j - a_2^j \tanh\left(\frac{r - a_3^j}{a_4^j}\right) - a_5^j \tanh\left(\frac{r - a_6^j}{a_7^j}\right), \quad (9)$$

to fit the surfactant profile at each time t^* for which we have data, where $t^* = j$, $j = 1, 2, \dots, 10$ s. This procedure generates coefficients a_1^j, \dots, a_7^j .

Next we create polynomial functions, $a_i^*(t^*)$, $i = 1, \dots, 7$, from the discrete values a_i^j , $j = 1, \dots, 10$ using *polyfit* in MATLAB, but with a restriction that the mass of the surfactant must be conserved. Since the numerical code requires nondimensional time $t = 0.5t^*$, we define $a_i(t) = a_i^*(2t)$, $i = 1, \dots, 7$. These functions define the surfactant concentration profiles that approximate the experimental data:

$$\Gamma(r, t) = a_1(t) - a_2(t) \tanh\left(\frac{r - a_3(t)}{a_4(t)}\right) - a_5(t) \tanh\left(\frac{r - a_6(t)}{a_7(t)}\right). \quad (10)$$

We update the height profile using the finite-difference scheme used in Sect. 4 with boundary conditions (3) and the surfactant concentration profile using (10):

$$h_j^{n+1} = h_j^n + \Delta t \frac{1}{r_j \Delta r} \left(\mathcal{F}_{j+1/2}^{n+1} - \mathcal{F}_{j-1/2}^{n+1} \right), \quad (11a)$$

$$\Gamma_j^{n+1} = a_1(t^{n+1}) - a_2(t^{n+1}) \tanh\left(\frac{r - a_3(t^{n+1})}{a_4(t^{n+1})}\right) - a_5(t^{n+1}) \tanh\left(\frac{r - a_6(t^{n+1})}{a_7(t^{n+1})}\right). \quad (11b)$$

The flux functions \mathcal{F}_j^n are described in the appendix.

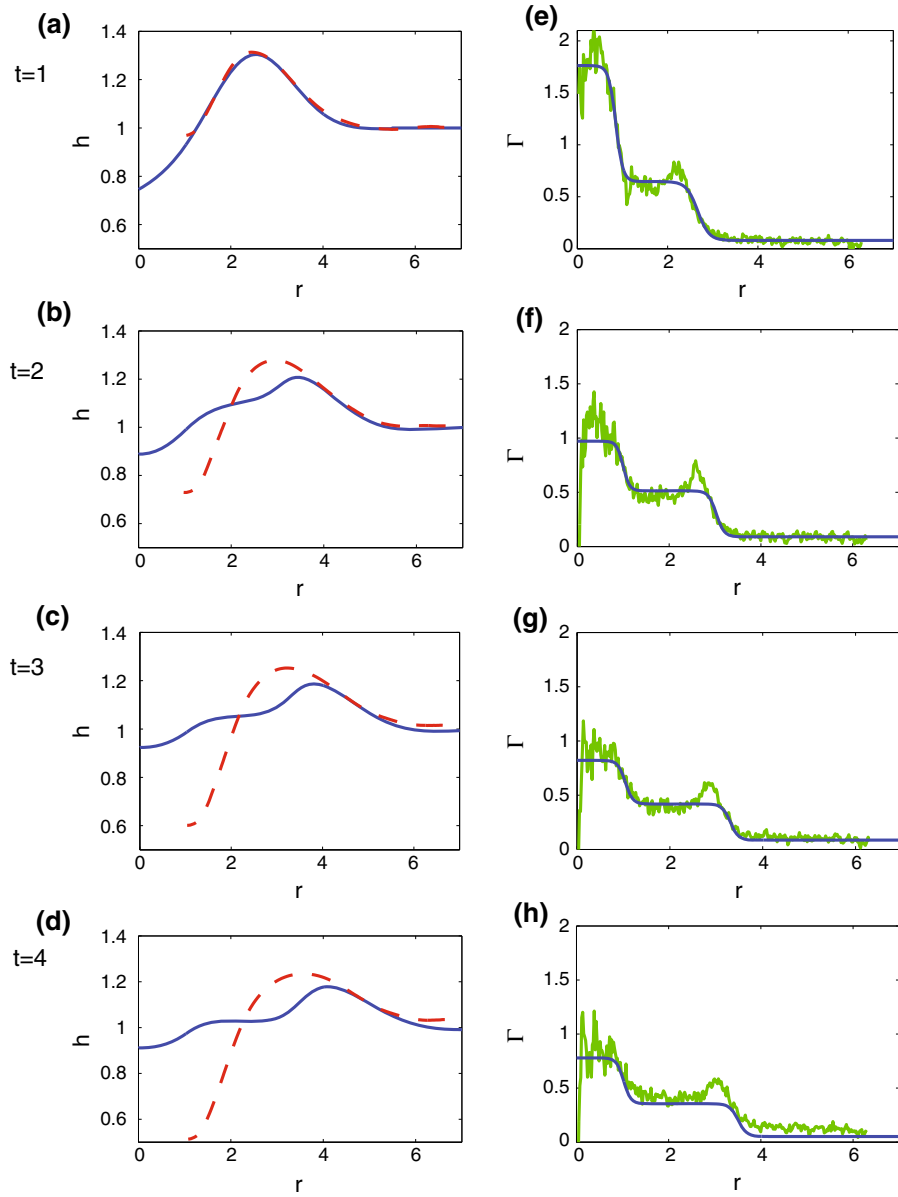
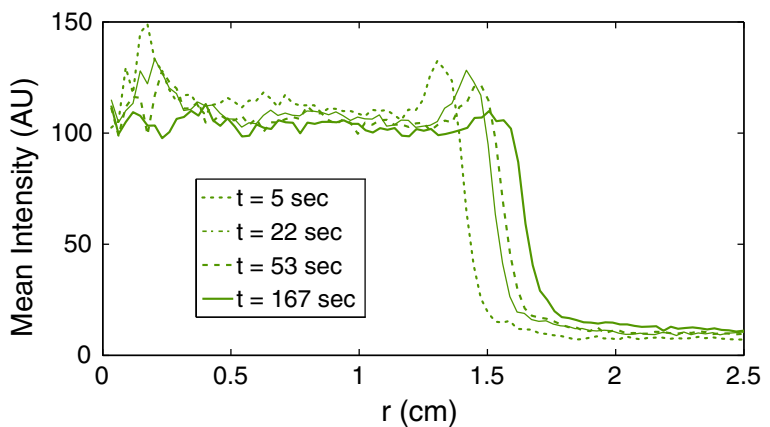


Fig. 9 **a–d** Comparison of surface height profiles $h(r)$ from numerical simulations (solid blue) and experimental data (dashed red). **e–h** Corresponding surfactant profiles from experiment, smoothed data (smooth blue) and raw data (noisy green). The profiles are shown at $t^* = 1, 2, 3, 4$ s. The experimental data correspond to IC6. (Color figure online)

In Fig. 9, we show simulation results using initial condition (4) and parameters $\beta = 0.5$, $\kappa = 0.5$. Note that this artificial value of κ is larger than the value suggested by the corresponding nondimensional grouping. Using this artificial value, we perform numerical experiments to explore how the height profile would develop for a surfactant profile similar to those observed in the experiment. This larger value of κ smooths the height profile, which otherwise would develop multiple, pronounced, persistent ridges because of the steep gradient in the surfactant concentration. Multiple ridges are observed at very early times in the simulations discussed in Sect. 4.2, but then the gradient in the surfactant is quickly smoothed. In this case, the ridge in the height profile from the surfactant gradient and that from the initial condition (due to the lifting of the ring) combine at a very early time and then propagate as

Fig. 10 Azimuthally averaged fluorescence intensity (in arbitrary units specific to our Andor camera) at a distance r from the center of the surfactant region, shown at representative times, taken from an experiment with IC4 ($\bar{\Gamma}_0^* < \Gamma_c$)



one. By contrast, in the experiment the surfactant distribution does not experience this smoothing, maintaining the steep gradients. Consequently, when the experimental values for the surfactant concentration are input into the height equation, a second ridge develops and persists. By increasing the capillarity parameter κ , the height profile is smoothed, and the numerical height profile becomes more similar to the experimental height profile.

The surface height profile simulated using this hybrid model captures key features of the height profile from the experiment. In particular, the location and slope of the outer slope of the ridge in the height profile are in agreement between the experiment and simulation. We conclude that the equation modeling surfactant molecule motion through passive transport by the surface fluid is fundamentally flawed; it is missing some physical or chemical properties that would generate the surfactant distributions observed in the experiment.

6 Monolayer surfactant concentration ($\bar{\Gamma}_0^* < \Gamma_c$)

Because the original model (2) was developed for use with monolayer concentrations of surfactants ($\bar{\Gamma}_0^* < \Gamma_c$), we conduct new experiments in this regime. In addition, these experiments help elucidate the discrepancies between model and experiment at the higher concentrations. Performing experiments at lower surfactant concentrations requires improvements of our earlier experimental techniques (Sect. 2) in order to visualize lower surfactant concentrations. We perform experiments starting from four different initial concentrations, IC1–IC4 in Table 2, all of which result in similar spreading dynamics, described in what follows. In no case do we find that the agreement with the model is improved over the $\bar{\Gamma}_0^* > \Gamma_c$ case: height profiles, surfactant distribution, and the spreading dynamics all significantly disagree with the model predictions.

6.1 Height profile and surfactant distribution

As illustrated in Fig. 2 and shown quantitatively in Fig. 10, the spreading region has an approximately uniform surfactant distribution throughout the lipid-covered area. The leading edge, located at r_0 , exhibits a sharp interface (approximately 0.5 mm wide, neglecting azimuthal corrugations) that does not broaden as the surfactant spreads outward. Instead, the overall concentration decreases throughout the lipid-covered region. These observations are in disagreement with the model, which predicts a monotonically decreasing profile (Fig. 6) with a gradual and broadening transition to $\Gamma = 0$ at r_0 (Figs. 10, 11, 12).

Figure 11 provides a comparison between the behavior of the fluid ridge in two regimes. For $\bar{\Gamma}_0^* > \Gamma_c$, the glycerin is pushed out by the surface tension gradient and forms a capillary ridge at the surfactant edge (panels a–e). As already discussed in Sect. 4.2, these two features travel outward together. This is consistent with simulations at high or low surfactant concentrations that show a fluid ridge propagating outward due to Marangoni forces. In

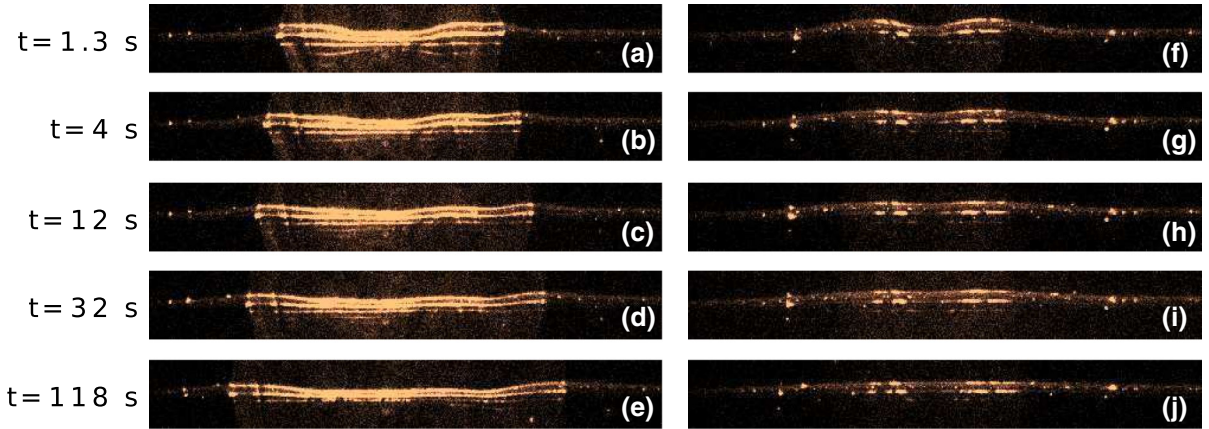
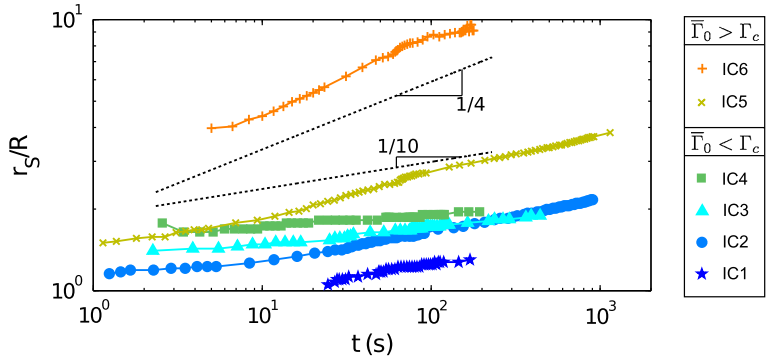


Fig. 11 Images comparing laser profile for two experiments with IC5 (**a–e**) ($\bar{\Gamma}_0^* > \Gamma_c$) and IC2 (**f–j**) ($\bar{\Gamma}_0^* < \Gamma_c$) at five different times. The uppermost bright line in each image is the reflection from the air–glycerin interface and is used to measure the free-surface height profile $h(t)$

Fig. 12 Spreading dynamics of location of leading edge of fluorescence intensity (r_0), scaled by ring radius R_0 . The dashed lines, corresponding to $t^{1/4}$ and $t^{1/10}$ spreading behavior, are shown for comparison



contrast, the experimental data in the $\bar{\Gamma}_0^* < \Gamma_c$ regime (panels **f–j**) show an initial ridge (due to the meniscus at the ring) collapsing rapidly in place and no discernible ridge propagating outward.

6.2 Spreading exponent

Given the significant differences between the observed and modeled $h(r, t)$ and $\Gamma(r, t)$, it is unsurprising that we observe the spreading dynamics to be quite different as well. In Fig. 12, we plot the position of the leading edge r_0 as a function of time, for experiments in both the monolayer regime of IC1–IC4 and for higher initial concentrations (IC5–IC6). For $\bar{\Gamma}_0^* < \Gamma_c$ (IC1–IC4) the dynamics all follow a form $r_0 \propto t^\alpha$, with $\alpha \lesssim 1/10$. Remarkably, this is reminiscent of Tanner's law for fluid spreading on a solid [37]. For slightly larger values of $\bar{\Gamma}_0^*$ (IC5), we observe faster surfactant spreading dynamics initially, but $r_0 \propto t^\alpha$, with $\alpha \approx 1/10$ at later times. This slow-spreading regime was not reached in the runs with much larger values of $\bar{\Gamma}_0^*$ (IC6) for which α remains close to $\alpha = 1/4$, as predicted in [6]. The decrease in α for low surfactant concentrations suggests a transition in the dynamics that is not covered by the model equations. The differing prefactors for the various runs is probably a result of variations in $\bar{\Gamma}_0^*$ due to some lipid molecules remaining on the ring after it lifts off, an effect that is more significant at lower concentrations.

7 Discussion

Current mathematical models that describe the dynamics of the free surface of a thin fluid layer subject to forces induced by variations in surface tension contain two key assumptions: (1) lubrication theory is valid, and (2) surfac-

tant molecules are advected along the fluid surface with negligible molecular diffusion. However, the dependence of surface forces on local variations in surfactant concentration is not completely settled, especially for larger concentrations. Due to the coupling between the motion of the underlying fluid and the spreading of surfactant molecules, it is crucial to compare results from simulations and experiments for both fluid motion (through surface deformations) and the dynamics of surfactant distribution.

In this paper, we compare model predictions to experiments that include the simultaneous visualization of the fluid height profile and the distribution of surfactant, both above and below the critical monolayer concentration Γ_c . In both cases, we find serious inconsistencies between the model and the experiments. The aspect ratio for the experiments is $H_0/R_0 \approx 0.1$, which justifies the use of the lubrication approximation; we have not verified the magnitude of the vertical velocity profile. At all initial concentrations [3, 33, 35], both above and below Γ_c , the spatial distribution of surfactants does not follow the smooth, monotonically decreasing profiles predicted by the model. At low surfactant concentrations ($\bar{\Gamma}_0^* < \Gamma_c$, for which the models were originally developed), the distribution is highly uniform, with a sharp interface at the leading edge. Second, spreading occurs much more slowly than is predicted by the model. For all experiments with $\bar{\Gamma}_0^* < \Gamma_c$, the spreading dynamics of the leading edge approximately follow a power law $r_0(t) \propto t^\alpha$, with $\alpha \lesssim 1/10$. This is significantly smaller than the $\alpha = 1/4$ predicted by the natural scaling in the model. Interestingly, this exponent is also markedly different from the exponent of 1/2 to 3/4 observed by Gaver and Grotberg [18] for oleic acid and by Bull et al. [1] for NBD-PC. In the former case, the measurement technique relies on the model for interpretation of experimental results, while in the latter the 2 mm fluid-layer thickness may be large enough that deviations from the lubrication approximation are significant. For $\bar{\Gamma}_0^* > \Gamma_c$, even though $\alpha \approx 1/4$, there is a mismatch by a factor of two between the timescales predicted in the model and observed in experiment. These inconsistencies are not resolved by changing assumptions concerning the initial distribution of surfactant. Moreover, if a measured $\Gamma(r, t)$ is incorporated directly into the lubrication model, then the timescale issue is no longer present because the spreading ridge is simply driven by the spreading surfactant. Since viscosity is the only unknown parameter in the timescale calculation, it is possible that *in situ* viscosity measurements under experimental conditions could resolve this issue and definitively fix the timescale. Another possibility is that timescale issues arise from the lubrication approximation's not being valid for fluid layers this thick.

One untested assumption is the functional form of the equations of state that have been considered to date. The lack of spreading ($\alpha \lesssim 1/10$ for very low concentrations) might indicate that the assumed $\sigma(\Gamma)$ equation of state is inadequate. If there were a value of Γ below which there was no longer a significant surface tension gradient, a lack of spreading would be expected. In fact, in static surface-pressure measurements of diolein, oleyl alcohol, and lecithin on water, such an effect has been observed [38]. Future work to make similar measurements for NBD-PC, potentially locating a second transition point, may clarify the reason for the reduction in spreading. Another possibility is that the passive transport model for surfactant distribution on a free surface is missing one or more effects that influence the dynamics of insoluble surfactant spreading on thin liquid films, such as that the capillarity or surface diffusion is dependent on the surfactant concentration, as studied in [39].

Acknowledgments We are grateful for support from the National Science Foundation under Grant DMS-0968258, DMS-0604047, DMS-0636590 RTG, and Research Corporations. In addition, we wish to thank Rachel Levy for valuable conversations concerning surfactant spreading.

Appendix

We summarize the finite-difference method used to generate numerical results for system (2). Simulations are conducted on a large interval $0 \leq r \leq R$. For simplicity, we consider uniformly distributed grid points $r_j = j\Delta r$, $j = 1, \dots, N$, where $\Delta r = R/N$. At each time $t_n = n\Delta t$, $n \geq 0$, let $h_j^n \approx h(r_j, n\Delta t)$ and $\Gamma_j^n \approx \Gamma(r_j, n\Delta t)$. We use the standard notation for spatial averages of $u_j^n = u(r_j, t_n)$,

$$\bar{u}_{j+1/2}^n \equiv \frac{u_{j+1}^n + u_j^n}{2}. \quad (12)$$

The numerical method is an implicit finite-difference scheme in conservative form:

$$h_j^{n+1} = h_j^n + \Delta t \frac{1}{r_j \Delta r} \left(\mathcal{F}_{j+1/2}^{n+1} - \mathcal{F}_{j-1/2}^{n+1} \right), \quad (13a)$$

$$\Gamma_j^{n+1} = \Gamma_j^n + \Delta t \frac{1}{r_j \Delta r} \left(\mathcal{G}_{j+1/2}^{n+1} - \mathcal{G}_{j-1/2}^{n+1} \right). \quad (13b)$$

The fluxes inherit the structure of the partial differential equation system (2) (note that we have dropped the $n+1$ superscript):

$$\mathcal{F}_{j+1/2} = \frac{1}{2} \mathcal{F}_{j+1/2}^A + \frac{1}{3} \beta \mathcal{F}_{j+1/2}^B + \frac{1}{3} \kappa \mathcal{F}_{j+1/2}^C, \quad (14a)$$

$$\mathcal{G}_{j+1/2} = \mathcal{G}_{j+1/2}^A + \frac{1}{2} \beta \mathcal{G}_{j+1/2}^B + \frac{1}{2} \kappa \mathcal{G}_{j+1/2}^C + \delta \mathcal{G}_{j+1/2}^D. \quad (14b)$$

The individual fluxes are expressed as

$$\mathcal{F}_{j+1/2}^A = \bar{r}_{j+1/2} (\bar{h}_{j+1/2})^2 \sigma' (\bar{\Gamma}_{j+1/2}) \frac{\Gamma_{j+1} - \Gamma_j}{\Delta r}, \quad (15a)$$

$$\mathcal{F}_{j+1/2}^B = \bar{r}_{j+1/2} (\bar{h}_{j+1/2})^3 \frac{h_{j+1} - h_j}{\Delta r}, \quad (15b)$$

$$\mathcal{F}_{j+1/2}^C = \bar{r}_{j+1/2} (\bar{h}_{j+1/2})^3 \frac{\mathcal{E}_{j+2} - \mathcal{E}_j}{2 \Delta r}, \quad (15c)$$

$$\mathcal{E}_{j+2} = \frac{h_{j+3} - 2h_{j+2} + h_{j+1}}{\Delta r^2} + \frac{1}{\bar{r}_{j+\frac{3}{2}}} \frac{h_{j+2} - h_{j+1}}{\Delta r}, \quad (15d)$$

$$\mathcal{G}_{j+1/2}^A = \bar{r}_{j+1/2} \bar{h}_{j+1/2} \bar{\Gamma}_{j+1/2} \sigma' (\bar{\Gamma}_{j+1/2}) \frac{\Gamma_{j+1} - \Gamma_j}{\Delta r}, \quad (15e)$$

$$\mathcal{G}_{j+1/2}^B = \bar{r}_{j+1/2} (\bar{h}_{j+1/2})^2 \bar{\Gamma}_{j+1/2} \frac{h_{j+1} - h_j}{\Delta r}, \quad (15f)$$

$$\mathcal{G}_{j+1/2}^C = \bar{r}_{j+1/2} (\bar{h}_{j+1/2})^2 \bar{\Gamma}_{j+1/2} \frac{\mathcal{E}_{j+2} - \mathcal{E}_j}{2 \Delta r}, \quad (15g)$$

$$\mathcal{G}_{j+1/2}^D = \bar{r}_{j+1/2} \frac{\Gamma_{j+1} - \Gamma_j}{\Delta r}, \quad (15h)$$

where $\mathcal{F}_{j+1/2}^B$ and $\mathcal{G}_{j+1/2}^B$ incorporate gravity, $\mathcal{F}_{j+1/2}^C$ and $\mathcal{G}_{j+1/2}^C$ capillarity, and $\mathcal{G}_{j+1/2}^D$ surface diffusion. In the hybrid model of Sect. 5, the values of Γ_j^n are derived from the experimental data, as described in that section. The height profile evolution can then be computed from Eq. (13a), and the companion equation (13b) is discarded. The boundary conditions corresponding to (3) are as follows:

$$h_1^{n+1} = h_0^{n+1}, \quad h_{-2}^{n+1} = h_2^{n+1}, \quad \Gamma_1^{n+1} = \Gamma_0^{n+1},$$

$$h_N^{n+1} = 1, \quad \Gamma_N^{n+1} = 0.$$

References

1. Bull JL, Nelson LK, Walsh JT, Glucksberg MR, Schurch S, Grotberg JB (1999) Surfactant-spreading and surface-compression disturbance on a thin viscous film. *J Biomech Eng-T ASME* 121:89–98
2. Dussaud AD, Matar OK, Troian SM (2005) Spreading characteristics of an insoluble surfactant film on a thin liquid layer: comparison between theory and experiment. *J Fluid Mech* 544:23–51
3. Fallest DW, Lichtenberger AM, Fox C, Daniels KE (2010) Fluorescent visualization of a spreading surfactant. *New J Phys* 12:73029
4. Gaver DP, Grotberg JB (1990) The dynamics of a localized surfactant on a thin-film. *J Fluid Mech* 213:127–148
5. Jensen OE (1994) Self-similar, surfactant-driven flows. *Phys Fluids* 6(3):1084–1094
6. Jensen OE, Grotberg JB (1992) Insoluble surfactant spreading on a thin viscous film: shock evolution and film rupture. *J Fluid Mech* 240:259–288

7. Grotberg JB (2011) Respiratory fluid mechanics. *Phys Fluids* 23(2):021301
8. Braun R (2012) Dynamics of the tear film. *Annu Rev Fluid Mech* 44:267–297
9. Jensen OE, Halpern D, Grotberg JB (1994) Transport of a passive solute by surfactant-driven flows. *Chem Eng Sci* 49(8):1107–1117
10. Evans PL, Schwartz LW, Roy RV (2000) A mathematical model for crater defect formation in a drying paint layer. *J Colloid Interface Sci* 227(1):191–205
11. Gundabala VR, Lei C, Ouzineb K, Dupont O, Keddie JL, Routh AF (2008) Lateral surface nonuniformities in drying latex films. *Aiche J* 54(12):3092–3105
12. Gundabala VR, Routh AF (2006) Thinning of drying latex films due to surfactant. *J Colloid Interface Sci* 303(1):306–314
13. Hanyak M, Darhuber AA, Ren M (2011) Surfactant-induced delay of leveling of inkjet-printed patterns. *J Appl Phys* 109(7):074905
14. Hanyak M, Sinz DKN, Darhuber AA (2012) Soluble surfactant spreading on spatially confined thin liquid films. *Soft Matter* 8(29):7660
15. Sinz DKN, Hanyak M, Zeegers JCH, Darhuber A (2011) Insoluble surfactant spreading along thin liquid films confined by chemical surface patterns. *Phys Chem Chem Phys* 13(20):9768–9777
16. Peterson ER, Shearer M (2011) Radial spreading of surfactant on a thin liquid film. *Appl Math Res Express* 2011(1):1–22
17. Ahmad J, Hansen R (1972) A simple quantitative treatment of the spreading of monolayers on thin liquid films. *J Colloid Interface Sci* 38(3):601–604
18. Gaver DP, Grotberg JB (1992) Droplet spreading on a thin viscous film. *J Fluid Mech* 235:399–414
19. Segur JB, Oberstar HE (1951) Viscosity of glycerol and its aqueous solutions. *Ind Eng Chem* 43(9):2117–2120
20. Sakata EK, Berg JC (1969) Surface diffusion in monolayers. *Ind Eng Chem Fund* 8:570–575
21. Wulf M, Michel S, Grundke K, del Rio OI, Kwok DY, Neumann AW (1999) Simultaneous determination of surface tension and density of polymer melts using axisymmetric drop shape analysis. *J Colloid Interface Sci* 210(1):172–181
22. Edmonstone BD, Matar OK, Craster RV (2006) A note on the coating of an inclined plane in the presence of soluble surfactant. *J Colloid Interface Sci* 293:222–229
23. Halpern D, Grotberg JB (1992) Transport of a localized soluble surfactant on a thin film. *J Fluid Mech* 237:1–11
24. Jensen OE, Grotberg JB (1993) The spreading of heat or soluble surfactant along a thin liquid film. *Phys Fluids A–Fluids* 5:58–68
25. Edmonstone BD, Matar OK, Craster RV (2004) Flow of surfactant-laden thin films down an inclined plane. *J Eng Math* 50(2–3):141–156
26. Levy R, Shearer M, Witelski TP (2007) Gravity-driven thin liquid films with insoluble surfactant: smooth traveling waves. *Eur J Appl Math* 18:679–708
27. Matar OK, Troian SM (1999) Spreading of a surfactant monolayer on a thin liquid film: onset and evolution of digitated structures. *Chaos* 9(1):141–153
28. Warner MRE, Craster RV, Matar OK (2004) Fingering phenomena created by a soluble surfactant deposition on a thin liquid film. *Phys Fluids* 16(8):2933–2951
29. Borgas MS, Grotberg JB (1988) Monolayer flow in an thin film. *J Fluid Mech* 193:151–170
30. Sheludko A (1966) Colloid chemistry. Elsevier, Amsterdam
31. Foda M, Cox RG (1980) The spreading of thin liquid films on a water-air interface. *J Fluid Mech* 101:33–57
32. Miner CS, Dalton NN (1953) Glycerol. American chemical society monograph series. Reinhold Publishing Corp, New York
33. Strickland SL, Hin M, Sayanagi MR, Gaebler C, Daniels KE, Levy R (2014) Self-healing dynamics of surfactant coatings on thin viscous films. *Phys Fluids* 26(4):042109
34. Shrive JDA, Brennan JD, Brown RS, Krull UJ (1995) Optimization of self-quenching response of nitrobenzoxadiazole dipalmitoylphosphatidylethanolamine in phospholipid membranes for biosensor development. *Appl Spectrosc* 49(3):304–313
35. Vogel MJ, Hirsa AH (2002) Concentration measurements downstream of an insoluble monolayer front. *J Fluid Mech* 472:283–305
36. Peterson ER, Shearer M (2012) Simulation of spreading surfactant on a thin liquid film. *Appl Math Comput* 218(9):5157–5167
37. Tanner LH (1979) The spreading of silicone oil drops on horizontal surfaces. *J Phys D Appl Phys* 12:1473–1484
38. Henderson DM (1998) Effects of surfactants on Faraday-wave dynamics. *J Fluid Mech* 365:89–107
39. Thiele U, Archer AJ (2012) Thermodynamically consistent description of the hydrodynamics of free surfaces covered by insoluble surfactants on high concentration. *Am Inst Phys* 24(10):102107